

www.acsanm.org Article

# Corona Phase Molecular Recognition of the Interleukin-6 (IL-6) Family of Cytokines Using nIR Fluorescent Single-Walled Carbon Nanotubes

Xiaojia Jin, Michael A. Lee, Xun Gong, Volodymyr B. Koman, Daniel J. Lundberg, Song Wang, Naveed A. Bakh, Minkyung Park, Juyao Ivy Dong, Daichi Kozawa, Soo-Yeon Cho, and Michael S. Strano\*



Cite This: ACS Appl. Nano Mater. 2023, 6, 9791–9804



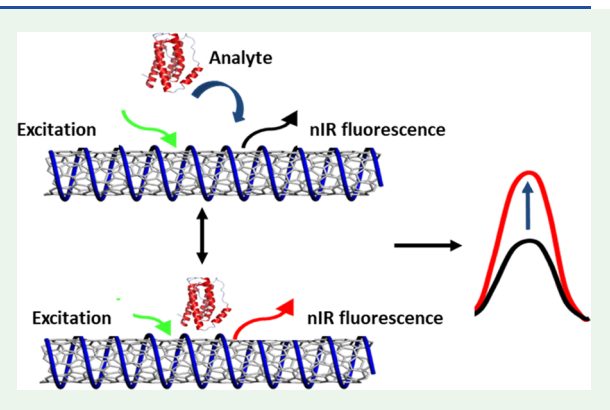
ACCESS

III Metrics & More

Article Recommendations

Supporting Information

ABSTRACT: The Interleukin-6 (IL-6) family of cytokines regulates inflammation and plays important roles in numerous biochemical pathways. Typically, cytokine levels are measured using enzyme-linked immunosorbent assay (ELISA) or western blot. However, these techniques usually require substantial processing time, cost, machinery, and specialist training. Understanding the fundamental molecular recognition mechanism of cytokines with synthetic substrates is key to developing new biomedical technologies such as assays, sensors, and therapeutics that overcome the above limitations. Herein, we use the corona phase molecular recognition (CoPhMoRe) approach to engineer new carbon nanotube constructs and study their binding to the inflammatory cytokines: IL-6, interleukin-11 (IL-11), ciliary neurotrophic factor (CNTF), and leukemia inhibitory factor (LIF). Library screening



identified two polymer-based CoPhMoRe constructs consisting of single-walled carbon nanotubes complexed with  $p(AA_{68}$ -rand- $BA_{16}$ -rand- $CD_{16}$ ) polymer (MK2) or  $p(SS_{80}$ -rand- $BS_{20}$ ) polymer (P14) corona phases. The resulting dissociation constants ( $K_D$ ) were 8.38 ng/mL and 16.7  $\mu$ g/mL, respectively, compared to that of the natural IL-6 receptor at ~0.32 ng/mL. In addition, the MK2 constructs showed a nonmonotonic response function upon binding with IL-6. Comparative binding experiments suggest that both constructs appear to recognize the axially aligned  $\alpha$ -helical structures present in the Interleukin-6 family. The findings from this study elucidate how nanoparticle interfaces, such as those produced by CoPhMoRe, can be designed to lock onto specific protein features. We find that the  $\alpha$ -helical structure of the IL-6 family of cytokines can enable facile molecular recognition, opening the door to new types of label-free, low-cost sensing technologies.

**KEYWORDS:** molecular recognition, single-walled carbon nanotube, fluorescent sensors, nanosensor, inflammation biomarker, interleukin-6

# 1. INTRODUCTION

Molecular recognition<sup>1</sup> events that selectively identify molecules of interest are central for research in cell signaling pathway studies, <sup>2,3</sup> early disease diagnosis, <sup>4-6</sup> and therapeutics development. <sup>7-9</sup> Currently, natural systems, such as antibodies, are the most common recognition sites. <sup>10</sup> However, they are prone to suffer from hydrolysis and degradation, <sup>8,11,12</sup> loss of activity after immobilization, <sup>13</sup> low tunability of binding affinity, <sup>14</sup> and have limited availability for a wide range of molecules. <sup>15,16</sup> Therefore, extensive research efforts have focused on designing synthetic analogues to natural recognition sites that recognize target analytes with high specificity. <sup>1,17–20</sup> One example of such synthetic recognition sites can be constructed with molecular imprinting, <sup>21–23</sup> which involves creating cavities in the polymer matrices using the target analyte as a template. The molecular imprinting method

has been successfully applied to various molecules, including both small molecules<sup>24</sup> and biological macromolecules.<sup>25,26</sup> However, this method lacks generalizability and is time-consuming to design a large library for screening. Additionally, substrates produced by molecular imprinting have a lower binding capacity when compared to antibodies and may suffer from incomplete template removal.<sup>24</sup> Other synthetic recognition constructs, such as self-assembled nanoparticles, <sup>5,27,28</sup> usually lack specificity and interact with the target analyte in a

Received: April 5, 2023 Accepted: May 12, 2023 Published: May 26, 2023





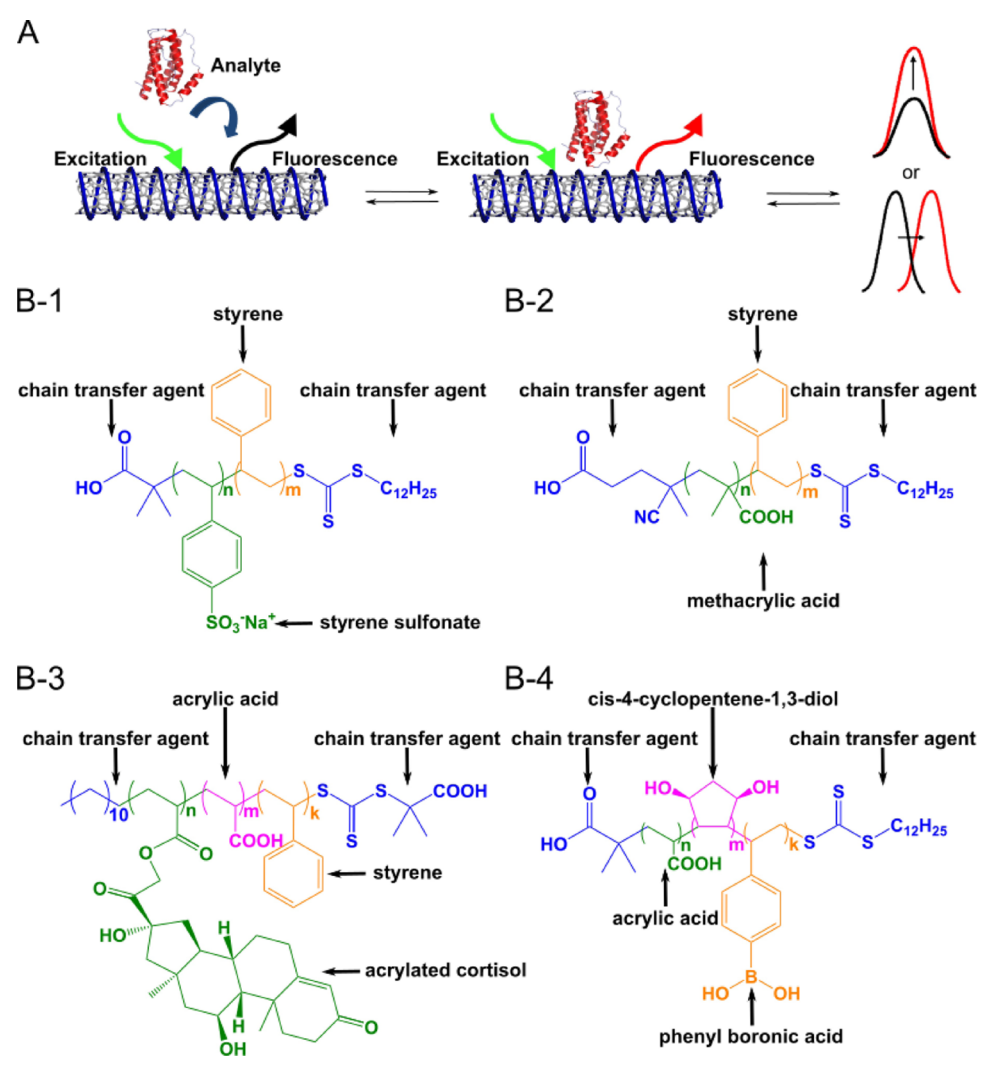


Figure 1. Design of corona phase molecular recognition constructs for IL-6 sensing. (A) Schematics of amphiphilic polymer-functionalized SWNT that modulates the fluorescence of carbon nanotubes. Upon incubation, the target molecule interacts with the corona phase, which induces a measurable intensity change and/or peak wavelength shift of the SWNT fluorescence. (B) Chemical structures of four amphiphilic polymer families selected for corona phase construction, where the hydrophobic components are colored orange, hydrophilic components are colored green and/or pink, and the RAFT agents are colored blue. (B-1) Styrene sulfonate—styrene derivative copolymers (P-series); (B-2) Methacrylic acid—styrene copolymers (I-series); (B-3) Templated steroid polymers (SM-series); and (B-4) acrylic acid—phenyl boronic acid—diol copolymers (MK-series).

nonspecific manner.<sup>29</sup> Finally, despite various efforts, there are currently no well-tested design rules regarding how synthetic substrates can be engineered to recognize specific features of important biomolecules.

In recent years, our group has developed the technique of corona phase molecular recognition (CoPhMoRe) to produce synthetic molecular recognition constructs at the interface of a nanoparticle surface (corona phase) that selectively binds a target analyte. These constructs are typically heteropolymers selected from a library of adsorbed phases complexed to create a unique nanoparticle-hybrid structure. In practice, a CoPhMoRe screen represents a high-throughput screening framework that identifies an optimal corona phase consisting of adsorbed polymers or surfactants at the nanoparticle surface, excluding molecular interactions with the nanoparticle other than the target analyte. Typically, carbon nanotubes (CNTs) are chosen as the underlying nanomaterial to host synthetic molecular recognition interfaces. CNT has emerged as a power nanosensor with distinct advantages for molecular recognition

of biological analytes.<sup>31–33</sup> Its high aspect ratio, large surface area-to-volume ratio, electrical conductivity, high chemical stability, and optical properties are of great benefit for sensing applications. For example, it has been developed as an optical sensor for neurotransmitters,<sup>34</sup> an electrochemical sensor for food safety,<sup>35</sup> and a field-effect device for viral detection.<sup>36</sup>

When applying the CoPhMoRe approach, we are particularly interested in semiconducting single-walled carbon nanotubes (SWNTs). Its high aspect ratio nanostructure guides polymer folding/catalyst fixation through supramolecular interaction.<sup>37</sup> In addition, SWNTs can also serve as a signal transducer for molecular recognition through a change in its band-gap photoluminescence.<sup>38</sup> Unlike traditional organic fluorophores, SWNTs do not photobleach,<sup>39</sup> which extends the lifetime of the fluorescence indefinitely. Furthermore, SWNTs fluoresce at near-infrared (nIR) wavelengths (900–1500 nm), which allows deeper tissues to be probed due to reduced tissue scattering and autofluorescence as well as lower absorption in the near-infrared window.<sup>38,40</sup>

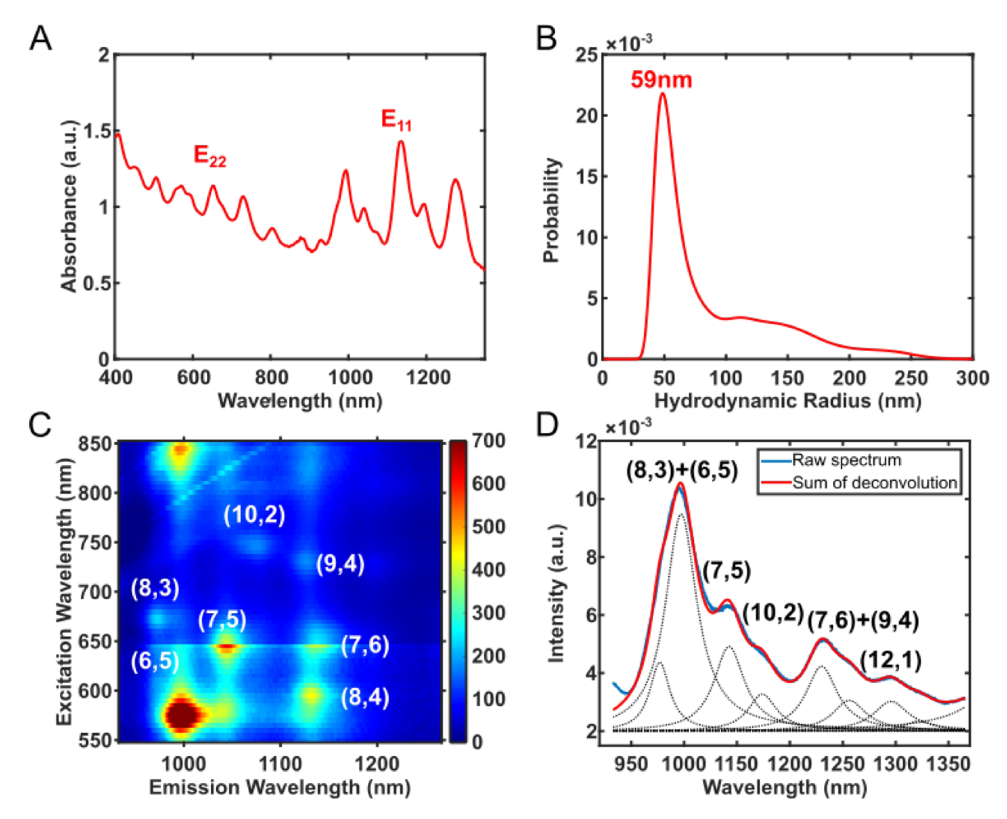


**Figure 2.** Characterization of example SWNT colloidal dispersions. (A) UV-Vis-nIR absorption spectrum of MK2-SWNT corona with distinct peaks of  $E_{11}$  and  $E_{22}$  transitions, indicating the successful isolation of individual SWNTs. (B) Hydrodynamic size distributions of individual tubes accessed using dark-field scattering microscopy, based on the Brownian motion of individual nanotubes. The results show a single population of MK2-SWNT corona with an average hydrodynamic radius of about 59 nm. (C) Excitation-emission profile of MK2-SWNT corona, where individually suspended SWNTs were illuminated with excitation wavelengths ranging from 550 to 850 nm, and the emission wavelengths between 930 and 1280 nm were recorded. Spectra were collected in intervals of 5 nm using an exposure time of 20 s. The profile illustrates the existence of local maxima in emission intensity, with the location of each maximum corresponding to a particular chirality of semiconducting carbon nanotubes labeled with a pair of integers. The artifact at 650 nm was caused by the tunable grating switch from the excitation source. (D) nIR emission spectrum of nanotubes under 785 nm excitation wavelength was fitted to quantify the contribution of each chirality: raw spectrum (blue curve), individual chirality contribution (dashed dark curves), and the sum of the individual peaks (red curves). Changes in emission spectra are used to quantify the interaction between analytes and corona phases.

Mechanistically, fluorescence emission of SWNTs can be selectively modulated by a target molecule binding to the corona in two ways: (1) modulation of the charge-transfer transitions and exciton relaxation mode, which induces an emission intensity change, 41,42 and (2) modulation of the effective dielectric constant, which induces an emission wavelength shift due to solvatochromism (Figure 1A).<sup>43</sup> The CoPhMoRe technique has proven effective in probing the realtime dynamics of various analytes in complex environments with high selectivity for extended periods, including animal models, 30,44 and more recently, living plants. 45-48 In addition, CoPhMoRe has demonstrated its versatility by successfully detecting various molecules, such as nitric oxide, 42,49 hydrogen peroxide, <sup>2</sup> vitamins, <sup>30</sup> neurotransmitters, <sup>50</sup> carbohydrates, <sup>51</sup> proteins, <sup>15,52,53</sup> small molecule pharmaceutical drugs, <sup>7,40</sup> and steroids. 44 However, further work is required to demonstrate the applicability of the CoPhMoRe technique to macromolecules, 15,52 such as cytokines, which is the subject of this work.

Interleukin-6 (IL-6), a protein ranging from 21 to 28 kDa in size, is composed of four  $\alpha$  helices and has three receptor sites. <sup>54–58</sup> The molecule is secreted by lymphoid cells and macrophages and plays an important role in inducing the final differentiation of B cells into antibody-producing cells. <sup>57,59</sup> IL-

6 is involved in a number of physiological processes, including inflammation, infection responses, neural functions, and healing processes.  $^{55-57,60-62}$  For instance, the apoptosis of neutrophils, recruitment of T lymphocytes, and B-cell differentiation all involve IL-6. Overexpression for genes upregulation IL-6 synthesis will disrupt the normal functions of human body. For a healthy human, the serum IL-6 level is around 4.2  $\pm$  5.86 pg/mL, and levels of IL-6 are similar in plasma and sweat, ranging from 5 to 15 pg/mL. Similar in plasma and sweat, ranging from 5 to 15 pg/mL. Accordingly 1000-fold increases in IL-6 levels have been observed in severe cases of infectious diseases such as COVID-19 and Influenza.

The IL-6 family cytokines, which include interleukin-11 (IL-11), ciliary neurotrophic factor (CNTF), and leukemia inhibitory factor (LIF),  $^{54,58}$  are structurally similar to IL-6 and share a common signaling receptor subunit glycoprotein 130 kDa (gp13) in their receptor complexes.  $^{54,58,74-76}$  The structure of the IL-6 family of cytokines is dominated by a four- $\alpha$ -helix bundle, which is anti-parallel and shares a common up-up-down-down topology. The IL-6 family cytokines have been implicated in numerous biochemical activities, including the regulation of the hepatic acute phase reaction, B-cell stimulation, and regulation of the balance metabolic and neural functions. Developing technology to

detect these molecules can aid in the study of their effects and subsequent relationship to disease processes, given the important roles of the IL-6 family of cytokines in numerous biochemical pathways.

In this work, we use CoPhMoRe technique to generate synthetic binding sites on fluorescent single-walled carbon nanotubes. The sites, or nanoparticle corona phases, are then tested for their ability to recognize specific features of the IL-6 family of cytokines as a homologous series of target analytes. Findings from this study elucidate how nanoparticle interfaces can be designed to lock onto specific protein features, particularly aligned  $\alpha$ -helical structures, to enable molecular recognition and new types of sensing technologies. The observed synthetic molecular recognition elements would also enhance the mechanistic understanding of the signaling pathways in human body, as well as facilitate the diagnosis and treatment of diseases.

## 2. RESULTS

2.1. Polymer Library Design, Construct Synthesis, and Characterization. SWNTs from the high-pressure carbon monoxide (HiPCo) process were suspended with a design library of 41 amphiphilic polymers capable of forming corona phases with SWNTs. The hydrophobic part of the polymer facilitates the adherence of SWNTs, while the hydrophilic part enhances SWNTs' colloidal stability in an aqueous environment where most biologically active molecules exist. The hydrophobic portion of the polymers consists of aromatic rings from styrene and its derivatives, which form strong  $\pi$ – $\pi$  stacking with the SWNT surface, while the hydrophilic portion is composed of functional monomers, such as acrylic acid, styrene sulfonate, and diols, which facilitate supramolecular interactions with target molecules. Four different families of styrene-based copolymers have been synthesized based on the monomer structures and the synthetic feasibility (Figure 1B): (1) styrene sulfonate-styrene derivative copolymers (P series);<sup>77</sup> (2) methacrylic acidstyrene copolymers (I-series),<sup>78</sup> which have shown specific molecular interaction with Vardenafil molecules previously;<sup>78</sup> (3) templated steroid polymers (SM-series), 44 consisting of acrylic acid, styrene, and acrylated cortisol (the template), which was believed to selectively interact with the template steroid; and (4) acrylic acid-phenyl boronic acid-diol copolymers (MK-series). The copolymers were chosen such that they have a variety of monomeric compositions and chain lengths to sample a range of free volumes and relative strength of binding to produce structurally diverse corona phases. In total, 14 copolymers of styrene and styrene sulfonate, 15 copolymers of template steroid, 8 copolymers of methacrylic acid-styrene, and 4 copolymers of acrylic acid-phenyl boronic acid-diol have been synthesized and formed corona phases with SWNT (Table S1).

The 41 selected polymers were synthesized using reversible addition—fragmentation chain transfer (RAFT) polymerization to achieve a narrow polydispersity. To screen against a panel of chiralities that had previously demonstrated various CoPh-MoRe responses, we used HiPCo SWNTs that contain more than 10 types of chirality. The polymer—SWNT constructs were then prepared by ultrasonication procedure of the polymer and SWNT mixtures in 1× phosphate-buffered saline (PBS), followed by ultracentrifugation to isolate individually dispersed SWNT from heavier aggregates. The supernatant was dialyzed against 1× PBS for 3 days to remove excess

unbound polymer. The resulting colloidal solutions were characterized by UV-Vis-nIR absorption spectroscopy (Figures 2A and S3-S6), and the successful suspension of the tubes was confirmed by the distinct  $E_{11}$  and  $E_{22}$  transition peaks. The concentration of the polymer-SWNT dispersion was then determined using the absorbance at 632 nm, with an extinction coefficient of 0.036 L mg<sup>-1</sup> cm<sup>-1</sup>.30 To measure particle size distributions within the dispersion, we use singleparticle tracking in a dark-field microscope and a Brownian motion analysis algorithm we previously developed, MANTA (maximum a posteriori nanoparticle tracking analysis).80 The hydrodynamic radius distributions of the SWNTs were measured using MANTA, and the expected unimodal population was observed (Figure 2B).81 The fluorescence of the polymer-SWNT construct as a function of excitation wavelength was measured using a supercontinuum laser coupled with a tunable grating. Our sample consisted of a mixture of SWNT structure populations or chiralities, each represented as a resonant emission peak on the excitationspectra map (Figure 2C).<sup>38</sup> Similarly, the sample can be excited via a single laser line at 785 nm, where the measured spectra is a linear combination of each of the individual SWNT chirality emissions (Figure 2D).<sup>38</sup> Commonly, SWNT chirality emissions are extracted via a fitting process, given the wellcharacterized line shapes and locations of each population.<sup>82</sup> We choose to combine two pairs of peaks (8, 3)/(6, 5) and (9, 3)4)/(7, 6) due to the ambiguity in the fitting process.

2.2. Screening for SWNT Corona Phases Targeting IL-**6.** We screened the constructed corona phases against a target library (Figure S7) consisting of 19 biologically active molecules related to inflammation processes, along with potential interfering molecules. To address the issue of nonspecific binding, we added strongly adsorbing bovine serum albumin (BSA) proteins as a positive control. The spectral change of the fluorescence emission of these coronas was examined following a 2 h incubation with the analytes (100  $\mu$ M for small molecules and 20  $\mu$ g/mL for proteins) in 0.5 M sodium chloride (NaCl) with PBS buffer at room temperature. Addition of 0.5 M NaCl was used to mimic the physiological environment where most interleukin exists, and the PBS buffer was used to reduce readout variabilities. PBS buffer containing 0.5 M NaCl was chosen as the negative control. To prevent confounding results from SWNT aggregation, we diluted the SWNT suspension to 1 mg/L and allowed it to equilibrate overnight before measurement.

The fitting of the emission spectra to extract the species of interest was performed using a modified Matlab script (Figure 2D).<sup>79</sup> No significant peak wavelength shifts were observed after analyte addition. Therefore, we used SWNT emission intensity change as an indication of molecular recognition in this work. In addition, we noticed a significant overlap between the (9, 4)/(7, 6) and (8, 3)/(6, 5) peaks. With those broad SWNT emission peaks, we decided to track the integrated area of emission for each chirality species of interest and combine the areas of the mentioned peaks to avoid potential artifacts introduced during the spectrum fitting process. In this case, we are interested in the following five SWNT species (Figure 2B): combined (8, 3)/(6, 5) peak area; (7, 5) peak area; (10, 2)peak area; combined (7, 6)/(9, 4) peak area; and (12, 1) peak area. The emission area after analyte incubation was compared to that of the negative control to calculate the normalized fluorescence response.

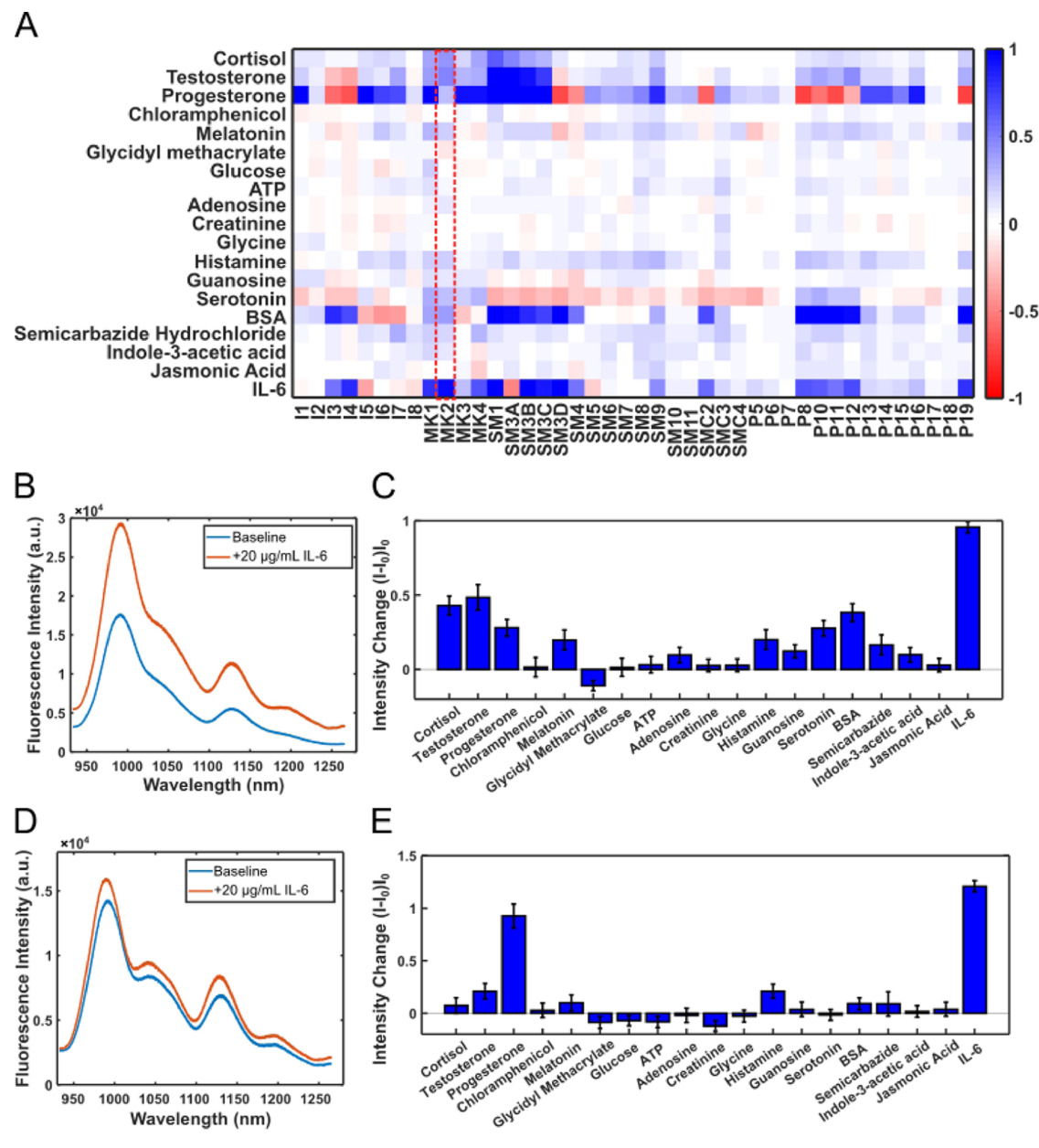


Figure 3. Summary of polymer library screening results. (A) Example heat map shows the normalized response for (9,4)/(7,6) SWNT chiralities wrapped with various coronas against the panel of analytes in  $1 \times PBS$ , where I and  $I_0$  are the fluorescent intensities with analyte and buffer addition, respectively. The SWNT concentration was 1 mg/L, while the analyte concentrations were  $100 \mu M$  for small molecules and  $20 \mu g/mL$  for proteins. Many constructs showed sensitivity to IL-6. The red box indicates selective responses to IL-6. In this case, we consider a construct selective if the difference between the IL-6 response and average responses to other molecules is larger than 3 times of the standard error. (B) nIR fluorescence emission of MK2 corona under 785 nm excitation increases in response to the addition of  $20 \mu g/mL$  IL-6. (C) Normalized response  $(I - I_0)/I_0$  of the combined (9, 4)/(7, 6) chiralities of MK2–SWNT construct (1 mg/L) against the panel of analytes. IL-6 induces approximately twice the change in the (9, 4) + (7, 6) chirality fluorescence intensity of the MK2 corona as compared to other analytes at an equivalent concentration (data presented as mean  $\pm$  SEM, n = 3). (D) nIR fluorescence emission of P14 corona increases in response to the 20  $\mu g/mL$  IL-6 addition. (E) Normalized response  $(I - I_0)/I_0$  of the (12, 1) chirality of P14–SWNT construct (1 mg/L) against the panel of analytes. The (12, 1) chirality of the P14–SWNT corona is selective toward IL-6 compared to other analytes except progesterone (data presented as mean  $\pm$  SEM, n = 3).

normalized response = 
$$\frac{I - I_0}{I_0}$$

where  $I_0$  and I are the integrated peak areas with analyte and buffer addition, respectively.

The normalized fluorescence responses of different chirality species are presented in the form of a heat map (Figures 3A and S8–S11): blue indicates a fluorescence increase or a "turn-on" response, whereas red indicates a fluorescence decrease or

a "turn-off" response. The saturation of the color represents the extent of the response. As shown in the heat maps (Figures 3A and S8–S11), while many of the 205 coronas showed a response to IL-6, only two constructs: MK2 - (9, 4 + 7, 6) and P14 - (12, 1) demonstrated the most promising selective responses (Figures 3A and S11). In this study, a construct is considered selective if the difference between the IL-6 response and the average responses to other molecules is

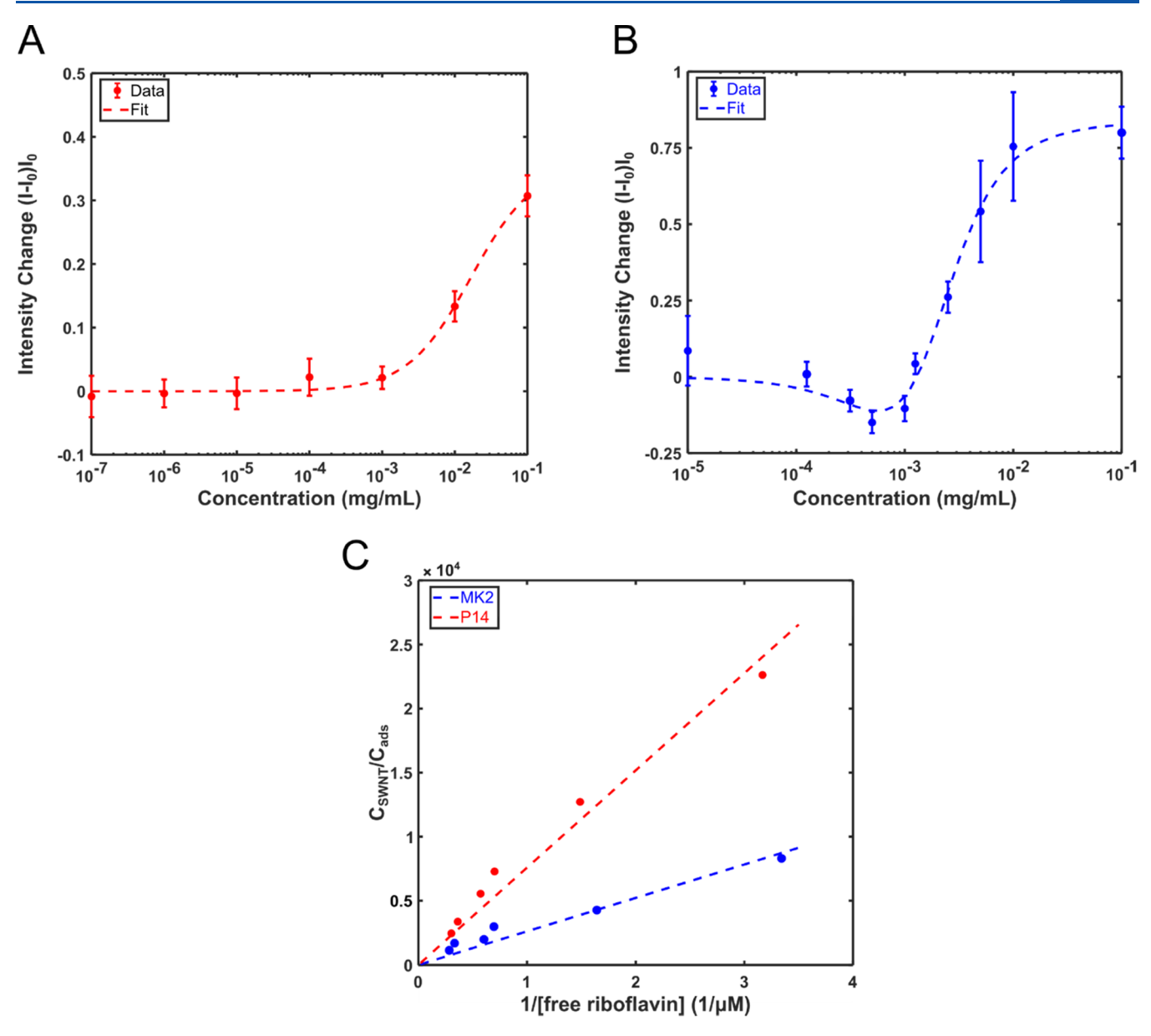


Figure 4. Dose-dependent response of the two IL-6 nanoconstructs. (A) Calibration of the dose-dependent response with the cooperative binding model as discussed in the text, showing that P14-wrapped nanoconstruct is sensitive to IL-6 from 10 to  $100 \mu g/mL$ ,  $R^2 = 0.99$  (data presented as mean  $\pm$  SEM, n = 3). (B) Nonmonotonic intensity responses between the MK2 construct and IL-6 are fitted to the two-step binding model, showing MK2-wrapped nanoconstruct sensitivity from 100 ng/mL to 0.1 mg/mL (data presented as mean  $\pm$  SEM, n = 3). (C) Calibration with MPA model informing the constructs' available surface area (blue: MK2–SWNT; red: P14–SWNT). The concentration ratio between SWNTs and adsorbed riboflavin ( $C_{\text{SWNT}}/C_{\text{ads}}$ ) is plotted against the inverse of the riboflavin concentration, where the linear slope is inversely proportional to the number of vacant sides on nanotubes. The calibration curves show that SWNTs with P14 corona have a larger slope indicating a smaller exposed surface area compared to the MK2 corona.

greater than 3 times of the standard deviation of the response to buffer addition.

The MK2 corona phase consists of HiPCo SWNTs wrapped by  $p(AA_{68}$ -rand- $BA_{16}$ -rand- $CD_{16})$  polymer, and the combined (9, 4) and (7, 6) chirality peak exhibited a 96% turn-on response to addition of 20  $\mu$ g/mL of IL-6 (Figure 3B,C), whereas the magnitude of the second-highest response to analytes in the screening library was 56%. The P14 corona phase consists of HiPCo SWNT wrapped by  $p(SS_{80}$ -rand- $BS_{20})$  polymer, and the (12, 1) chirality peak exhibited a 121% turn-on response to IL-6 addition (Figure 3D,E). Notably, both constructs showed negligible response to the BSA protein, suggesting that the interaction between the two

corona phases and IL-6 is likely structurally specific. We also prepared polymers with the same monomeric unit but varying monomeric compositions as MK2 and P14 to suspend SWNTs and examined the nIR spectral change of the corresponding corona construct. The result suggests that molecular recognition is strongly dependent on the specific hydrophilic—hydrophobic composition of the corona phase. For example, p(SS75-rand-BS25), composed of the same monomers as P14, elicited less than 5% turn-on response upon addition of 20  $\mu$ g/mL of IL-6 but exhibited strong interaction (~106% turn-on response) with an identical concentration of BSA protein (Figure S12). Therefore, we confirmed that recognition was not due to the interaction between a specific

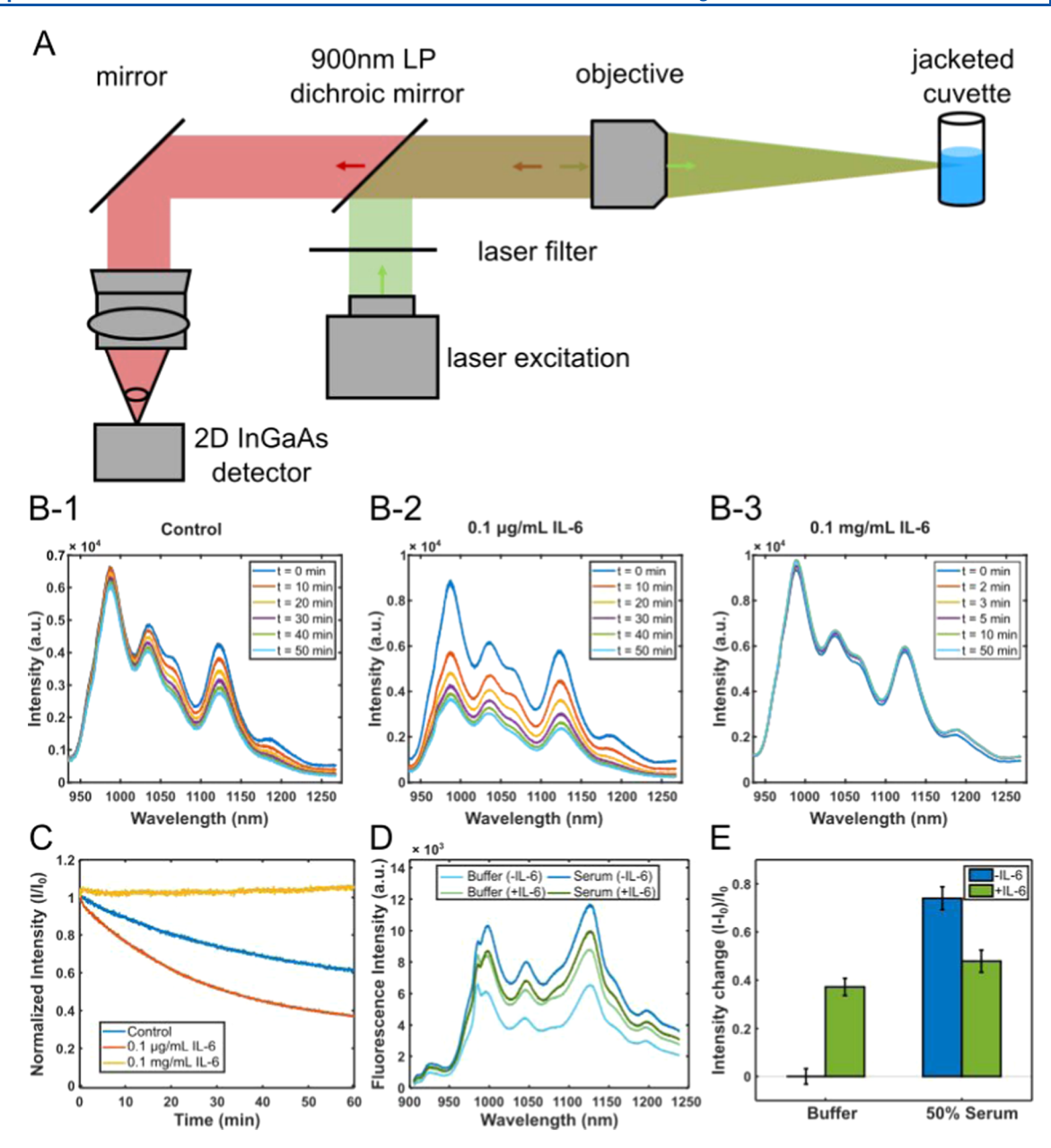


Figure 5. Dynamics and compatibility of the MK2 construct in a complex environment. (A) Schematic of the jacketed cuvette setup to measure the fluorescence intensity response continuously. The excitation laser beam passed through a neutral density filter, followed by a long-distance objective, to focus the light onto a quartz cuvette. Sample solution was added to the jacketed cuvette at 25 °C. The solution was stirred at a constant rate of 1200 rpm. The sample fluorescence emission was collected after passing through the 900 nm long pass filter and imaged on a liquid nitrogen-cooled 1D InGaAs detector. (B) Fluorescence emission spectra of 1 mg/L MK2–SWNT, to which buffer (B-1), 0.1  $\mu$ g/mL IL-6 (B-2), or 0.1 mg/mL IL-6 (B-3) was added after the SWNT fluorescence reached a steady state (t = 0 min). We set the point when we added the buffer/ analyte solution to be time zero in the graph. (C) Combined (9, 4)/(7, 6) chirality fluorescence emission peak area of 1 mg/L MK2 construct over time, to which buffer, 0.1  $\mu$ g/mL IL-6, or 0.1 mg/mL IL-6 was added. Data taken from panel (B). (D, E) Photophysical response of the MK2 construct in a complex environment. (D) Fluorescence emission spectra of 1 mg/L MK2–SWNT before and after the addition of 20  $\mu$ g/mL IL-6 in 0.5 M NaCl buffer condition (light color) and 50% serum environment (dark color). (E) Integrated normalized response of the MK2–SWNT construct (1 mg/mL) as compared to the SWNT diluted in 1× PBS. In this case,  $I_0$  was the nanotube emission intensity in 1× PBS buffer solution, while I is the emission intensity of SWNT with (1) 0.5 M NaCl; (2) 20  $\mu$ g/mL IL-6 in 0.5 M NaCl; (3) 50% serum; or (4) 20  $\mu$ g/mL IL-6 in 50% serum. Intensity of 0.5 M NaCl in 1× PBS was used as a negative control (data presented as mean  $\pm$  SEM, n = 3).

monomeric component and IL-6. All of these observations support the existence of specific molecular recognition between the two corona phases and IL-6.

2.3. Concentration-Dependent Photophysical Response of CoPhMoRe Constructs. To study the SWNT constructs' potential as a quantitative tool, we calculated the normalized response  $(I\text{-}I_0)/I_0$  at different analyte concen-

trations (Figures S15 and S16) to construct dose—response curves (Figure 4A,B). The two potential candidate MK2 and P14 constructs were again chosen for calculation. The tested analyte concentration ranged from 1 ng/mL to 1 mg/mL, and the SWNT fluorescence intensity saturated at 0.1–1 mg/mL. We used a kinetic adsorption model to model the calibration

curves, specifically assuming a first-order reversible reaction between the analyte (A) and available binding sites  $(\theta)$ .

$$A + \theta \rightleftharpoons A\theta \tag{1}$$

where  $[A\theta]$  is the surface concentration of analyte-bound sites. The resulting equilibrium for this reaction is

$$K_{\mathbf{A}} = \frac{[A\theta]}{[A][\theta]} \tag{2}$$

Assuming a type I isotherm, and the SWNT fluorescence response is proportional to the  $A\theta/\theta_{\rm tot}$  ratio,

$$\frac{I_0 - I}{I_0} = \alpha \frac{[A\theta]}{[\theta_{\text{tot}}]} = \alpha \frac{[A]K_A}{[A]K_A + 1} = \beta \frac{[A]}{[A] + K_D}$$
(3)

where  $K_D$  is the dissociation constant and is the inverse of the equilibrium constant  $K_A$ .

The dose-dependent response of the P14 corona fits with this model well (Figure 4A), and the  $K_{\rm D}$  is calculated to be 16.7  $\mu {\rm g/mL}$ , and  $\beta$  is calculated to be 0.36.

One intriguing finding was the nonmonotonic two-stage response of the MK2 construct (Figure 4B): fluorescence decreased at a very low analyte concentration and then increased with a higher concentration. A new analyte-SWNT corona binding scheme with two-step binding (eq 10) was proposed. With a low concentration of IL-6, the analyte binds to an empty site on the nanotube surface and induces a decrease of SWNT fluorescence.

$$A + \theta \stackrel{K_1}{\leftrightarrow} \theta_{\Lambda} \quad \text{(turn off)} \tag{4}$$

With a higher concentration of IL-6, it tends to interact with an existing bound site, thus increasing the SWNT fluorescence

$$A + \theta_A \stackrel{K_2}{\leftrightarrow} \theta_{AA}$$
 (turn on) (5)

where  $K_1$  and  $K_2$  are the equilibrium constants for the two reactions and adsorption site balance can be calculated as follows:

$$\theta_{\text{tot}} = \theta + \theta_{\text{A}} + \theta_{\text{AA}} \tag{6}$$

$$\theta_{\text{tot}} = \theta + [A]\theta K_1 + [A]\theta_A K_2 \tag{7}$$

$$\theta_{\text{tot}} = \theta + K_1[A]\theta + [A]^2 K_1 K_2 \theta \tag{8}$$

Assuming the fluorescence response is determined by the  $\theta_{\rm A}/\theta_{\rm tot}$  and  $\theta_{\rm AA}/\theta_{\rm tot}$  ratio,

$$\frac{\Delta I}{I_0} = \frac{\beta_1 \theta_A + \beta_2 \theta_{AA}}{\theta_{tot}} \tag{9}$$

$$\frac{\Delta I}{I_0} = \frac{\beta_1 K_1[A] + \beta_2[A]^2 K_1 K_2}{1 + K_1[A] + [A]^2 K_1 K_2} \tag{10}$$

Experimental data fit the model well ( $R^2 = 0.98$ ), and the parameters were calculated to be  $\beta_1 = -129.6$ ,  $\beta_2 = 0.84$ ,  $K_1 = 3.05 \text{ (mg/mL)}^{-1}$ , and  $K_2 = 119 282.4 \text{ (mg/mL)}^{-1}$ .

If used for sensing, the current constructs, P14 and MK2, would have a detection limit of 3.91 and 1.75  $\mu g/mL$ , respectively. These values were calculated by adding the intensity change of the nanoconstruct from the addition of only buffer ( $S_{blank}$ ) and 3 times the standard deviation ( $\sigma_{blank}$ ) of the response as the noise level.

We hypothesize that the two-stage binding interaction specific to the MK2 construct is due to a higher amount of exposed surface area of the nanotube, which allows a second IL-6 molecule to bind to a previously bound IL-6 molecule and form a dimeric structure, which is a common phenomenon for IL-6.58,83 The accessible surface area of the two potential constructs was measured using a newly developed molecular probe adsorption (MPA) technique,84 which involves the adsorption of a quenchable fluorescent riboflavin dye to the exposed surface of SWNTs via hydrophobic interaction. The extent of fluorescence quenching is proportional to the amount of adsorbed riboflavin and thus the exposed SWNT surface area, which can be quantified by calibrating the emission intensity of riboflavin with a type I Langmuir isotherm. The governing equation is derived as  $\frac{C_{\text{SWNT}}}{C_{\text{ads}}} = \frac{K_{\text{D}}}{q} \frac{1}{C_{\text{probe}}} + \frac{1}{q}$ , where  $C_{SWNT}$  is the concentration of SWNTs,  $C_{ads}$  is the concentration of adsorbed riboflavin,  $C_{probe}$  is the concentration of free riboflavin,  $K_D$  is the dissociation constant of riboflavin adsorption, and q is the number of vacant carbon atom.<sup>84</sup> Accordingly, the concentration ratio between SWNTs and adsorbed riboflavin  $(C_{SWNT}/C_{ads})$  is plotted against the inverse of the free riboflavin concentration (Figure 4C), and the linear slope is inversely proportional to the number of vacant sides on nanotubes. The results suggest a higher available surface area  $(q/K_D)$  of the MK2 construct  $(3.8 \times 10^3)$  $M^{-1}$ ) compared to that of the P14 construct  $(1.3 \times 10^3 M^{-1})$ , which is consistent with our initial hypothesis. In contrast,

DNA-wrapped carbon nanotubes commonly employed for detecting small molecule analytes usually have a smaller

exposed surface area  $(q/K_D)$ , ranging from 700 to 1000 M<sup>-1.84</sup>

2.4. IL-6 Interaction Dynamics and Compatibility in **Complex Environments.** The MK2 construct was chosen to further study its IL-6 binding in a complex environment to simulate potential applications in a point-of-care diagnostic device. The real-time dynamic responses of the construct to analyte addition were measured using a jacketed cuvette setup that maintained the sample at a constant temperature (Figure 5A). The signal readout was performed in a standard fluorescence configuration. Briefly, the excitation source passed through a neutral density filter, followed by a long-distance objective, to focus the light onto a quartz cuvette. MK2-SWNT was added to the jacketed cuvette with the temperature set to 25 °C. The solution was stirred under a constant rate of 1200 rpm, bringing fresh SWNTs into the focal volume. After fluorescence measurement reached a steady state, buffer solution (final conc.: 0.5 M NaCl in 1× PBS) or IL-6 (final conc.: 0.1  $\mu$ g/mL or 0.1 mg/mL) was then added to the SWNT dispersion. The addition of buffer solution served as a negative control to account for potential signal drifting caused by analyte addition and laser fluence effect.85 The change of the SWNT emission spectra under continuous 785 nm laser excitation was recorded every 3 s until a new steady state was reached (Figure 5B). Compared to the control, a decrease of SWNT response was observed when a lower concentration of IL-6 was added, and a fast increase of the fluorescence response was observed when a higher concentration of IL-6 was added (Figure 5C). These results further validate the nonmonotonic response between MK2 corona and IL-6 (Figure 4B). The time to reach 90% of the final nIR intensity change  $(\tau_{90})$  was observed to be 5.56 min with 0.1 mg/mL IL-6 addition (Figure 5C). The fast dynamic observed shows promise for applications that require sensing results within

several minutes.

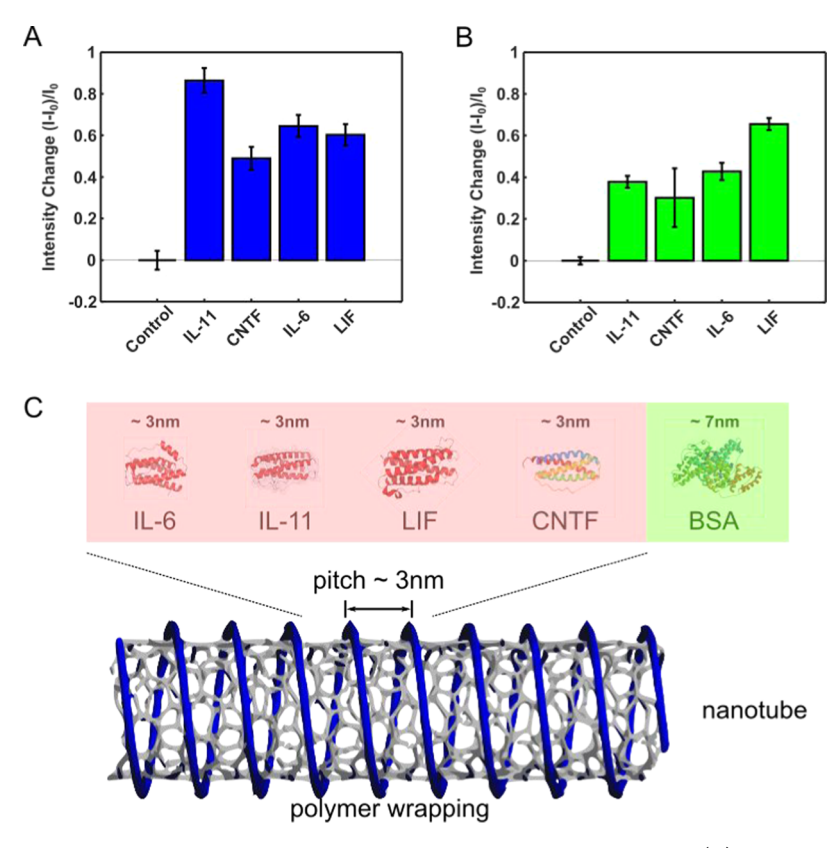


Figure 6. Investigation of the molecular recognition mechanism between corona constructs and IL-6. (A) Normalized response of the integrated intensity of MK2–SWNT constructs (1 mg/L) in response to addition of different IL-6 family cytokines (20  $\mu$ g/mL). Data presented as mean  $\pm$  SEM, n = 3. (B) Normalized response of the integrated intensity of P14–SWNT constructs (1 mg/L) in response to the addition of different IL-6 family cytokines (20  $\mu$ g/mL). Data presented as mean  $\pm$  SEM, n = 3. Both constructs exhibit similar responses to IL-6 and other IL-6 family cytokines, confirming that the interaction between the corona structure and the aligned α-helix structure is the key to molecular recognition. (C) Schematic of proposed interaction between the SWNT corona and the IL-6 family cytokines, where the pitch of the MK2 helical wrapping onto the SWNT surface matches the length of the α-helix structure of the cytokines. The SWNT is colored silver, the polymer is colored blue, and the cytokine molecules are shaded in red, whereas BSA molecule is shaded in green. An aligned four-helix bundle structure is observed in the IL-6 family proteins but not in BSA.

The photophysical response of the MK2 construct in biofluid was further assessed in the presence of pooled human serum as the target medium (Figure 5D,E). We introduced commercially available serum samples from pooled human donors at a final concentration of 50% v/v to the MK2-SWNT dispersion. The integrated intensity change of the whole spectrum was used to determine the fluorescence response to maximize the amount of signal measured. The results showed that the MK2 construct exhibited a turn-off response to IL-6 addition in 50% serum, whereas it displayed a turn-on response in buffer condition. The attenuation of the photophysical response in serum seems to arise from the increased baseline fluorescence with the serum background ( $\sim$ 74% turn-on compared to buffer). One possible explanation for future exploration may be that the difference in the ionic strength between the pooled human serum and the PBSbuffered 0.5 M NaCl solution leads to the disparity of the baseline fluorescence, highlighting the need to control environmental factors in SWNT-based assays. Nevertheless, there was still a discernible intensity difference between the serum only and IL-6 added serum sample, demonstrating the potential of the MK2 construct for IL-6 detection applications.

**2.5.** Proposed Mechanism of IL-6 Interaction and Investigation of Specificity. We propose that the specific interaction between IL-6 and the two corona phases can be attributed to two factors: the specific corona conformation of

polymer chains on the SWNT surface and the structure of the IL-6 molecule.83 Specifically, we hypothesize that when a polymer approaches the SWNT surface, it gradually wraps around the SWNT and rearranges itself to form an energyminimizing configuration. The resulting configuration creates a binding pocket that can recognize molecules of similar size and shape to that of the binding pocket. When a target molecule is much larger than the binding pocket, steric hindrance prevents it from approaching the SWNT surface closely enough to have a strong influence on the SWNT fluorescent readout. Conversely, if a target molecule is much smaller than the binding pocket, it can move around freely without being constrained or properly oriented for specific interactions. Additionally, the larger size of the binding pocket may allow other molecules to enter and interfere with the interaction between the target molecule and the corona phase. We suggest that the binding pocket of the MK2-SWNT and P14-SWNT constructs matches the size and shape of the aligned  $\alpha$ -helix structure of the IL-6 molecule. To validate this hypothesis, we evaluated the photophysical response of the two constructs to other IL-6 family cytokines, including Interleukin-11 (IL-11), 86 leukemia inhibitory factor (LIF),87 and ciliary neurotrophic factor (CNTF), 88 which also possess the four-helix bundle structure with up-up-down-down topology (Figure 6C). Both corona phases displayed similar spectral changes when interacting with IL-6 and other cytokines with an aligned  $\alpha$ - helix structure (Figure 6A,B). In contrast, BSA (Figure 6C) has an unaligned  $\alpha$ -helix structure that differs in size and shape from the IL-6 family cytokines and does not induce a commensurate fluorescence response (Figure 3C,E).

To further elucidate this proposition, we also investigated the conformation of the polymer wrapping onto the carbon nanotube. Assuming that the polymers form a helical structure with a specific pitch around the nanotube, 90,91 we calculated the pitch of the wrapping using a Hamiltonian function based on surface binding energy and polymer persistence length.<sup>90</sup> We examined (9,4) and (7,6) SWNT chiralities, which were used in the MK2 constructs and showed the most specific recognition. Their nanotube diameters were 0.91 and 0.89 nm, respectively. A polymer persistence length between 0.9 and 1.8 nm was required for the polymer molecule to favor adsorption onto the nanocylinder surface. 90 The persistence length of styrene sulfonate as measured in a 0.5 M NaCl solution is around 1.5 nm, 92 and the persistence length of poly-o-bromostyrene (1.65 nm) also falls into this range, 93 which confirms the existence of an energy-minimization polymer wrapping around the nanotube surface. Based on these parameters, the optimal pitch was predicted to be around 3.5 nm<sup>90</sup> for a tightly wrapped helical configuration. Similarly, the optimal pitch of the P14-(12,1) construct was determined to be around 3.0 nm. 90 In addition, helical wrapping was assumed to calculate the minimum pitch value in the calculation above, which provides insights into the allowable size of the target analyte that would dock into the binding pocket on the SWNT surface. Further analysis of the IL-6 structure reveals that each  $\alpha$ -helix structure in the  $\alpha$ -helices bundle is 20–25 residues in length. Since an  $\alpha$ -helix has  $\sim$ 3.6 amino acid residues per turn, and each turn of  $\alpha$ -helix has a pitch value around 0.55 nm, <sup>94,95</sup> the total length for each bundle is calculated to be around 3.0 nm. This length matches well with the predicted helical pitch of the corona phase-suggesting that IL-6 molecules could fit neatly within the warped corona phase, potentially interlocking with the styrenic wrapping of the nanotube (Figure 6C).

# 3. DISCUSSIONS AND CONCLUSIONS

Understanding the molecular recognition of IL-6 and IL-6 family cytokines is crucial for the advancement of new biomedical technologies, including sensors, therapeutics, and purification methods. In this work, we have demonstrated selective molecular recognition of IL-6 using polymerfunctionalized single-walled carbon nanotubes. By screening the fluorescence intensity change of a library of polymerwrapped SWNT induced by the interaction with a panel of inflammatory molecules, we discovered two corona phase constructs capable of specifically recognizing IL-6: MK2-SWNT and P14-SWNT. Both constructs exhibited a dosedependent response. The P14-IL-6 binding followed the typical kinetic adsorption model with a first-order reversible reaction, and MK2-IL-6 interaction revealed a two-stage sequential binding mechanism with the IL-6 homodimer formation, which was also confirmed through kinetic experiments. Finally, we tested the response of the MK2 construct to IL-6 in the presence of serum, which is a common medium used in the context of IL-6 measurement in healthcare. These findings demonstrate how corona phase-driven nanoparticle interfaces can be engineered to target specific protein structures as a paradigm of synthetic molecular recognition.

The current study focuses on a proof-of-concept demonstration of selective recognition of IL-6 with polymer-

functionalized carbon nanotubes. In its current form, a central limitation of the MK2 construct for biomedical applications is its low sensitivity. The limit of detection of the MK2 construct is in the  $\mu$ g/mL range, while the physiologically relevant IL-6 level is around single-digit pg/mL. In comparison, recent advances in technology have led to the development of stochastic sensors, which demonstrated a detection limit in the fg/mL range, even lower than standard methods, such as ELISA assay (pg/mL range). 96-98 One method to bring the LOD down by at least 3 orders of magnitude is by immobilization of the SWNT construct and probing at a single-particle level. Previous work in our group has demonstrated DNA-wrapped SWNT to exhibit single-molecule sensitivity to the inflammatory molecule nitric oxide after immobilization. 42,99 We believe similar experiments can be performed with the MK2 construct to improve its sensitivity. In addition, a hardware design that allows amplification of the sensor response with improved signal-to-noise (SNR) ratio could address this issue. Preliminary studies using an amplified photodetector (Figure S19) compared to the spectrophotometer used in this work exhibits promises that the sensor LOD would be further brought down to a physiologically relevant one, enabling applications for rapid detection of inflammation.

Furthermore, future work will also focus on elucidating the mechanism of such molecular recognition interaction. More indepth experimental characterization of the polymer wrapping onto the nanotube surface may shed light on the corona phase conformation, including potential regular structures responsible for binding events. Combined with simulations, we should then potentially gain details that would enable more structurally guided approaches for molecular recognition design.

# 4. METHODS

**4.1. Materials.** Raw single-walled carbon nanotubes (SWNT) produced by the HiPCO process were purchased from NanoIntegris and used without further processing (Batch HR27-104). All other chemicals were purchased from Sigma Millipore.

4.2. Polymer Synthesis and Characterization. The amphiphilic polymers used to disperse the SWNTs in aqueous solution were synthesized using reversible addition-fragmentation chain transfer (RAFT) polymerization, using 2-(dodecylthiocarbonothioylthio)-2methylpropionic acid (DDMAT) as the RAFT agent and 2,2'azobis(2-methylpropionitrile) (AIBN) as the initiator. MEHQ in acrylic acid and 4-tert-butylcatechol in monomers were removed by passing through columns packed with inhibitor removers. Trioctylammonium hydrochloride (TOA-HCL) for styrene sulfonatestyrene derivative copolymers (P-series) synthesis 100 was prepared according to Liu et al. 77 Acrylation of cortisol for the synthesis of templated steroid polymers (SM-series) was performed following a previously reported reaction scheme.<sup>44</sup> All other monomers were used as purchased. Monomer ratios and their ratio against DDMAT and AIBN were tuned for different polymer compositions (Table S1). For example, to synthesize the p(AA<sub>68</sub>-rand-BA<sub>16</sub>-rand-CD<sub>16</sub>) polymer (MK2) for screening, 24.1 mg of DDMAT (1 equiv), 2.2 mg of AIBN (0.2 equiv), 729.1 mg of acrylic acid (AA) (153 equiv), 352.3 mg of 3vinyl phenyl boronic acid (36 equiv), and 171.6 mg of cis-4cyclopentene-1,3-diol (36 equiv) were dissolved in 7.4 mL of dioxane. After the reaction, the mixture was added dropwise into 300 mL of diethyl ether to precipitate out the polymer. The precipitate was collected through filtration and redissolved in methanol. The solution was then precipitated in diethyl ether twice more to remove the unreacted monomer. The polymer powder was then dried under vacuum for 3 days and stored at -20 °C.

NMR spectra of purified polymers were obtained by dissolving polymers in methanol- $d_4$  to a concentration of 30 mg/mL. The polymer structure was examined by  $^1H$  NMR using a Bruker AVANCE III-400 NMR Spectrometer (Figures S1 and S2).

- 4.3. Polymer-SWNT Suspension and Characterization. 5 mg of HiPCO SWNT and 50 mg of polymers were mixed in 5 mL of 1× PBS. The solution pH was adjusted to 7.4 using 1 M NaOH. The mixture was sonicated for 10 min in a water bath and ultra-sonicated (QSonica) with a 6 mm probe tip (Cole-Parmer) for 1 h at 10 W in an ice bath. The resulting suspension was ultracentrifuged (Beckman Coulter, SW 35 Ti rotor) at 155 000 rcf for 4 h at 20 °C. The supernatant (top 80%) was collected and dialyzed against 1× PBS for 5 days using 100 kDa cutoff Float-a-Lyzer devices (Spectrum Labs) with buffer replacements thrice daily to remove free polymers. UV-Vis-nIR absorption spectra (Shimadzu UV-3101PC) were obtained using 1 cm path length quartz cuvettes (Starna). The mass concentration of the SWNT was determined using an extinction coefficient of  $\varepsilon_{632}$  = 0.036 mg/(L cm). The particle size was measured by a dark-field scattering microscope from Malvern Instruments Ltd. (NanoSight LM10) with a 405 nm laser. The measurement was carried out with 30 s exposure time for each collection, and the results were averaged over 31 collections.
- 4.4. High-Throughput Sensor Screening. High-throughput screening of the nanosensor library against the analyte panel was performed using a customized nIR microscope, which consists of a Zeiss Axio Vision inverted microscope body with a 20× objective coupled to an Acton SP2500 spectrometer and a liquid nitrogencooled InGaAs 1D detector (Princeton Instruments). Dialyzed SWNT dispersion was diluted in 1× PBS and was allowed to equilibrate overnight at room temperature. For screening, analytes were first diluted in PBS with 1 M NaCl and then mixed with an equal volume of SWNT dispersion to reach the final desired concentration. In a 96-well plate, SWNT dispersion (1 mg/mL) and analyte solution (100  $\mu$ M for small molecule analytes and 20  $\mu$ g/mL for protein analytes) were mixed in a final volume of 200  $\mu$ L in 1× PBS and incubated for 2 h at room temperature. The nIR fluorescence spectra of the samples from 950 to 1250 nm were obtained in triplicate under 785 nm photodiode laser illumination (400 mW, B&W Tek Inc.). The 2D excitation-emission spectra were collected using the same InGaAs detector with a supercontinuum laser as the excitation source (NKT Photonics). The SWNT emission intensities at different excitation wavelengths were then corrected using the laser excitation power at the corresponding wavelength. Exposure time varied from 0.5 to 8 s, depending on the SWNT corona phases. The fluorescence spectra were deconvoluted into individual peaks corresponding to single SWNT chiralities according to a previously reported algorithm.<sup>79</sup> Peak position and intensities of each sensor-analyte pair were compared to the sensor-blank negative control to calculate the sensor response.
- **4.5. Molecular Probe Adsorption (MPA) Surface Area Measurement.** The free surface area of the polymer-wrapped SWNTs was estimated according to the molecular probe adsorption technique. <sup>84</sup> Briefly, riboflavin was dissolved in nanopore water in a concentration range from 0 to 5  $\mu$ M, and its fluorescence emission was measured (Varioskan flash spectral scanning multimode microplate reader, Thermo Varioskan). Riboflavin was excited at 460 nm, and emission was collected from 510 to 540 nm, with a 2 nm step size. Deflection of the riboflavin fluorescence was measured in the presence of 10 mg/mL polymer—SWNT dispersion. The free surface area was then estimated from the fluorescence difference according to Park et al. <sup>84</sup>
- **4.6. Continuous Fluorescence Emission Monitoring.** Fluorescence emission was collected using a custom-made nIR setup, with continuous laser excitation (785 nm photodiode laser, 450 mW, B&W Tek Inc.) focused into a jacketed quartz cuvette equipped with a stir bar and a temperature controller set to 25 °C. The power at the sample was attenuated by adding neutral density filters (Thorlabs) in the excitation beam path. The SWNT fluorescence emission is collected after passing through a 900 nm long pass filter and sent to a PI Acton SP2500 spectrometer and imaged on a liquid nitrogen-

cooled 1D InGaAs detector (Princeton Instruments). For cuvette measurement, 2 mL of SWNT—analyte mixture at the desired concentration was added to the jacketed cuvette. The stirring was set to 1200 rpm. The sample was imaged (3 s exposure) for about 30 min to allow for equilibrium.

## ASSOCIATED CONTENT

# Supporting Information

The Supporting Information is available free of charge at https://pubs.acs.org/doi/10.1021/acsanm.3c01525.

Polymer library characterization, corona phase dispersion characterization, chirality-dependent fluorescence response, and representative raw fluorescence spectra and images (PDF)

## AUTHOR INFORMATION

## **Corresponding Author**

Michael S. Strano — Department of Chemical Engineering, Massachusetts Institute of Technology, Cambridge, Massachusetts 02139, United States; orcid.org/0000-0003-2944-808X; Email: strano@mit.edu

## **Authors**

- Xiaojia Jin Department of Chemical Engineering, Massachusetts Institute of Technology, Cambridge, Massachusetts 02139, United States; orcid.org/0000-0002-0694-5799
- Michael A. Lee Department of Chemical Engineering, Massachusetts Institute of Technology, Cambridge, Massachusetts 02139, United States
- Xun Gong Department of Chemical Engineering, Massachusetts Institute of Technology, Cambridge, Massachusetts 02139, United States; oorcid.org/0000-0003-4168-2768
- Volodymyr B. Koman Department of Chemical Engineering, Massachusetts Institute of Technology, Cambridge, Massachusetts 02139, United States; orcid.org/0000-0001-8480-4003
- Daniel J. Lundberg Department of Chemical Engineering, Massachusetts Institute of Technology, Cambridge, Massachusetts 02139, United States
- Song Wang Disruptive and Sustainable Technologies for Agricultural Precision IRG, Singapore-MIT Alliance for Research and Technology, Singapore 138602, Singapore
- Naveed A. Bakh Department of Chemical Engineering, Massachusetts Institute of Technology, Cambridge, Massachusetts 02139, United States
- Minkyung Park Department of Chemical Engineering, Massachusetts Institute of Technology, Cambridge, Massachusetts 02139, United States
- Juyao Ivy Dong Department of Chemical Engineering, Massachusetts Institute of Technology, Cambridge, Massachusetts 02139, United States
- Daichi Kozawa Department of Chemical Engineering, Massachusetts Institute of Technology, Cambridge, Massachusetts 02139, United States
- Soo-Yeon Cho School of Chemical Engineering, Sungkyunkwan University, Suwon 16419, Republic of Korea; orcid.org/0000-0001-6294-1154

Complete contact information is available at: https://pubs.acs.org/10.1021/acsanm.3c01525

#### **Author Contributions**

X.J., M.A.L., X.G., and M.S.S. formulated concepts and experimental designs. X.J., M.A.L., S.W., J.I.D., and M.P. designed the polymer library, performed the synthesis, and performed sensor characterization. X.J. and N.A.B. performed the sensor kinetic measurement. X.G. and V.B.K. aided in optical instrumentation and data analysis. D.J.L. performed the inverse-CoPhMoRe calculation. M.S.S., D.K., and S.-Y.C. contributed to data interpretation. The manuscript was written with contributions from all of the listed authors.

#### Notes

The authors declare no competing financial interest.

### ACKNOWLEDGMENTS

The authors are grateful for financial support from Amgen Inc. This research was also partially supported by the King Abdullah University of Science & Technology (OSR-2015 Sensors 2707) and the NSF Biosensing Program, under Award Number 2124194. M.P is grateful for the support of the Samsung scholarship. X.J. acknowledges support from Mathworks Inc. through the Mathworks Engineering Fellowship. The authors also acknowledge H. Lee, A. Zeng, G. Xue, J. Schacherl, S. Gibson, and L. Vega at Amgen for their constructive comments, guidance, and support.

#### REFERENCES

- (1) Mahon, C. S.; Fulton, D. A. Mimicking Nature with Synthetic Macromolecules Capable of Recognition. *Nat. Chem.* **2014**, *6*, 665–672.
- (2) Jin, H.; Heller, D. A.; Kalbacova, M.; Kim, J. H.; Zhang, J.; Boghossian, A. A.; Maheshri, N.; Strano, M. S. Detection of Single-Molecule H2 O2 Signalling from Epidermal Growth Factor Receptor Using Fluorescent Single-Walled Carbon Nanotubes. *Nat. Nanotechnol.* **2010**, *5*, 302–309.
- (3) Voskuil, J. L. A. The Challenges with the Validation of Research Antibodies. *F1000Research* **2017**, *6*, No. 161.
- (4) Xiang, Y.; Lu, Y. Using Personal Glucose Meters and Functional DNA Sensors to Quantify a Variety of Analytical Targets. *Nat. Chem.* **2011**, *3*, 697–703.
- (5) Kumar, A.; Sun, S. S.; Lees, A. J. Directed Assembly Metallocyclic Supramolecular Systems for Molecular Recognition and Chemical Sensing. *Coord. Chem. Rev.* **2008**, 252, 922–939.
- (6) Kumar, P.; Sobhanan, J.; Takano, Y.; Biju, V. Molecular Recognition in the Infection, Replication, and Transmission of COVID-19-Causing SARS-CoV-2: An Emerging Interface of Infectious Disease, Biological Chemistry, and Nanoscience. *NPG Asia Mater.* **2021**, *13*, No. 14.
- (7) Son, M.; Mehra, P.; Nguyen, F. T.; Jin, X.; Koman, V. B.; Gong, X.; Lee, M. A.; Bakh, N. A.; Strano, M. S. Molecular Recognition and In Vivo Detection of Temozolomide and 5-Aminoimidazole-4-Carboxamide for Glioblastoma Using Near-Infrared Fluorescent Carbon Nanotube Sensors. ACS Nano 2023, 17, 240.
- (8) Chames, P.; Van Regenmortel, M.; Weiss, E.; Baty, D. Therapeutic Antibodies: Successes, Limitations and Hopes for the Future. *Br. J. Pharmacol.* **2009**, *157*, 220–233.
- (9) Zhu, G.; Zheng, J.; Song, E.; Donovan, M.; Zhang, K.; Liu, C.; Tan, W. Self-Assembled, Aptamer-Tethered DNA Nanotrains for Targeted Transport of Molecular Drugs in Cancer Theranostics. *Proc. Natl. Acad. Sci. U.S.A.* **2013**, *110*, 7998–8003.
- (10) Köhler, G.; Milstein, C. Continuous Cultures of Fused Cells Secreting Antibody of Predefined Specificity. *Nature* **1975**, 256, 495–497
- (11) Beck, A.; Wurch, T.; Bailly, C.; Corvaia, N. Strategies and Challenges for the next Generation of Therapeutic Antibodies. *Nat. Rev. Immunol.* **2010**, *10*, 345–352.

- (12) Vlasak, J.; Ionescu, R. Fragmentation of Monoclonal Antibodies. *MAbs* **2011**, *3*, 253.
- (13) Shen, M.; Rusling, J. F.; Dixit, C. K. Site-Selective Orientated Immobilization of Antibodies and Conjugates for Immunodiagnostics Development. *Methods* **2017**, *116*, 95–111.
- (14) Haywood, J.; Mozziconacci, O.; Allegre, K. M.; Kerwin, B. A.; Schöneich, C. Light-Induced Conversion of Trp to Gly and Gly Hydroperoxide in IgG1. *Mol. Pharmaceutics* **2013**, *10*, 1146–1150.
- (15) Bisker, G.; Dong, J.; Park, H. D.; Iverson, N. M.; Ahn, J.; Nelson, J. T.; Landry, M. P.; Kruss, S.; Strano, M. S. Protein-Targeted Corona Phase Molecular Recognition. *Nat. Commun.* **2016**, *7*, No. 10241.
- (16) Jayasena, S. D. Aptamers: An Emerging Class of Molecules That Rival Antibodies in Diagnostics. *Clin. Chem.* **1999**, *45*, 1628–1650
- (17) Irshad, M.; Iqbal, N.; Mujahid, A.; Afzal, A.; Hussain, T.; Sharif, A.; Ahmad, E.; Athar, M. M. Molecularly Imprinted Nanomaterials for Sensor Applications. *Nanomaterials* **2013**, *3*, 615–637.
- (18) Späth, A.; Knig, B. Molecular Recognition of Organic Ammonium Ions in Solution Using Synthetic Receptors. *Beilstein J. Org. Chem.* **2010**, *6*, No. 32.
- (19) Langton, M. J.; Beer, P. D. Rotaxane and Catenane Host Structures for Sensing Charged Guest Species. *Acc. Chem. Res.* **2014**, 47, 1935–1949.
- (20) Shetty, D.; Khedkar, J. K.; Park, K. M.; Kim, K. Can We Beat the Biotin—Avidin Pair?: Cucurbit[7]Uril-Based Ultrahigh Affinity Host—Guest Complexes and Their Applications. *Chem. Soc. Rev.* **2015**, *44*, 8747—8761.
- (21) Alexander, C.; Davidson, L.; Hayes, W. Imprinted Polymers: Artificial Molecular Recognition Materials with Applications in Synthesis and Catalysis. *Tetrahedron* **2003**, *59*, 2025–2057.
- (22) Saylan, Y.; Akgönüllü, S.; Yavuz, H.; Ünal, S.; Denizli, A. Molecularly Imprinted Polymer Based Sensors for Medical Applications. *Sensors* **2019**, *19*, No. 279.
- (23) Cieplak, M.; Kutner, W. Artificial Biosensors: How Can Molecular Imprinting Mimic Biorecognition? *Trends Biotechnol.* **2016**, 34, 922–941.
- (24) Willner, I.; Shlyahovsky, B.; Zayats, M.; Willner, B. DNAzymes for Sensing, Nanobiotechnology and Logic Gate Applications. *Chem. Soc. Rev.* **2008**, *37*, 1153–1165.
- (25) Wulff, G. Molecular Imprinting in Cross-Linked Materials with the Aid of Molecular Templates— A Way towards Artificial Antibodies. *Angew. Chem., Int. Ed.* **1995**, 34, 1812–1832.
- (26) Lim, K. F.; Zin, A. M.; Romano, E.; Wanless, E. J.; Holdsworth, C. I. Advances and Challenges in the Design and Synthesis of Molecularly Imprinted Microspheres. *Mol. Imprinted Catal.* **2016**, 55–77
- (27) Grzelczak, M.; Vermant, J.; Furst, E. M.; Liz-Marzán, L. M. Directed Self-Assembly of Nanoparticles. *ACS Nano* **2010**, *4*, 3591–3605.
- (28) Hung, A. M.; Micheel, C. M.; Bozano, L. D.; Osterbur, L. W.; Wallraff, G. M.; Cha, J. N. Large-Area Spatially Ordered Arrays of Gold Nanoparticles Directed by Lithographically Confined DNA Origami. *Nat. Nanotechnol.* **2009**, *5*, 121–126.
- (29) Budhathoki-Uprety, J.; Shah, J.; Korsen, J. A.; Wayne, A. E.; Galassi, T. V.; Cohen, J. R.; Harvey, J. D.; Jena, P. V.; Ramanathan, L. V.; Jaimes, E. A.; Heller, D. A. Synthetic Molecular Recognition Nanosensor Paint for Microalbuminuria. *Nat. Commun.* **2019**, *10*, No. 9.
- (30) Zhang, J.; Landry, M. P.; Barone, P. W.; Kim, J.-H.; Lin, S.; Ulissi, Z. W.; Lin, D.; Mu, B.; Boghossian, A. A.; Hilmer, A. J.; Rwei, A.; Hinckley, A. C.; Kruss, S.; Shandell, M. A.; Nair, N.; Blake, S.; Şen, F.; Şen, S.; Croy, R. G.; Li, D.; Yum, K.; Ahn, J.-H.; Jin, H.; Heller, D. A.; Essigmann, J. M.; Blankschtein, D.; Strano, M. S. Molecular Recognition Using Corona Phase Complexes Made of Synthetic Polymers Adsorbed on Carbon Nanotubes. *Nat. Nanotechnol.* **2013**, *8*, 959.
- (31) Ferrier, D. C.; Honeychurch, K. C. Carbon Nanotube (CNT)-Based Biosensors. *Biosensors* **2021**, *11*, No. 486.

- (32) Meskher, H.; Mustansar, H. C.; Thakur, A. K.; Sathyamurthy, R.; Lynch, I.; Singh, P.; Han, T. K.; Saidur, R. Recent Trends in Carbon Nanotube (CNT)-Based Biosensors for the Fast and Sensitive Detection of Human Viruses: A Critical Review. *Nanoscale Adv.* **2023**, *5*, 992–1010.
- (33) Dai, B.; Zhou, R.; Ping, J.; Ying, Y.; Xie, L. Recent Advances in Carbon Nanotube-Based Biosensors for Biomolecular Detection. *TrAC, Trends Anal. Chem.* **2022**, *154*, No. 116658.
- (34) Pan, J.; Li, F.; Choi, J. H. Single-Walled Carbon Nanotubes as Optical Probes for Bio-Sensing and Imaging. *J. Mater. Chem. B* **2017**, *5*, 6511–6522.
- (35) Zhao, Q.; Gan, Z.; Zhuang, Q. Electrochemical Sensors Based on Carbon Nanotubes. *Electroanalysis* **2002**, *14*, 1609–1613.
- (36) Zamzami, M. A.; Rabbani, G.; Ahmad, A.; Basalah, A. A.; Al-Sabban, W. H.; Nate Ahn, S.; Choudhry, H. Carbon Nanotube Field-Effect Transistor (CNT-FET)-Based Biosensor for Rapid Detection of SARS-CoV-2 (COVID-19) Surface Spike Protein S1. *Bioelectrochemistry* **2022**, *143*, No. 107982.
- (37) Nurazzi, N. M.; Asyraf, M. R. M.; Khalina, A.; Abdullah, N.; Sabaruddin, F. A.; Kamarudin, S. H.; Ahmad, S.; Mahat, A. M.; Lee, C. L.; Aisyah, H. A.; Norrrahim, M. N. F.; Ilyas, R. A.; Harussani, M. M.; Ishak, M. R.; Sapuan, S. M. Fabrication, Functionalization, and Application of Carbon Nanotube-Reinforced Polymer Composite: An Overview. *Polymers* **2021**, *13*, No. 1047.
- (38) Bachilo, S. M.; Strano, M. S.; Kittrell, C.; Hauge, R. H.; Smalley, R. E.; Weisman, R. B. Structure-Assigned Optical Spectra of Single-Walled Carbon Nanotubes. *Science* **2002**, 298, 2361–2366.
- (39) Wray, S.; Cope, M.; Delpy, D. T.; Wyatt, J. S.; Reynolds, E. O. R. Characterization of the near Infrared Absorption Spectra of Cytochrome Aa3 and Haemoglobin for the Non-Invasive Monitoring of Cerebral Oxygenation. *Biochim. Biophys. Acta* 1988, 933, 184–192.
- (40) Koman, V. B.; Bakh, N. A.; Jin, X.; Nguyen, F. T.; Son, M.; Kozawa, D.; Lee, M. A.; Bisker, G.; Dong, J.; Strano, M. S. A Wavelength-Induced Frequency Filtering Method for Fluorescent Nanosensors in Vivo. *Nat. Nanotechnol.* **2022**, *17*, 643–652.
- (41) Satishkumar, B. C.; Brown, L. O.; Gao, Y.; Wang, C. C.; Wang, H. L.; Doorn, S. K. Reversible Fluorescence Quenching in Carbon Nanotubes for Biomolecular Sensing. *Nat. Nanotechnol.* **2007**, *2*, 560–564.
- (42) Zhang, J.; Boghossian, A. A.; Barone, P. W.; Rwei, A.; Kim, J. H.; Lin, D.; Heller, D. A.; Hilmer, A. J.; Nair, N.; Reuel, N. F.; Strano, M. S. Single Molecule Detection of Nitric Oxide Enabled by d(AT)15 DNA Adsorbed to near Infrared Fluorescent Single-Walled Carbon Nanotubes. J. Am. Chem. Soc. 2011, 133, 567–581.
- (43) Choi, J. H.; Strano, M. S. Solvatochromism in Single-Walled Carbon Nanotubes. *Appl. Phys. Lett.* **2007**, *90*, No. 223114.
- (44) Lee, M. A.; Wang, S.; Jin, X.; Bakh, N. A.; Nguyen, F. T.; Dong, J.; Silmore, K. S.; Gong, X.; Pham, C.; Jones, K. K.; Muthupalani, S.; Bisker, G.; Son, M.; Strano, M. S. Implantable Nanosensors for Human Steroid Hormone Sensing In Vivo Using a Self-Templating Corona Phase Molecular Recognition. *Adv. Healthcare Mater.* **2020**, 9, No. 2000429.
- (45) Lew, T. T. S.; Koman, V. B.; Silmore, K. S.; Seo, J. S.; Gordiichuk, P.; Kwak, S. Y.; Park, M.; Ang, M. C. Y.; Khong, D. T.; Lee, M. A.; Chan-Park, M. B.; Chua, N. H.; Strano, M. S. Real-Time Detection of Wound-Induced H2O2 Signalling Waves in Plants with Optical Nanosensors. *Nat. Plants* **2020**, *6*, 404–415.
- (46) Lew, T. T. S.; Park, M.; Cui, J.; Strano, M. S. Plant Nanobionic Sensors for Arsenic Detection. *Adv. Mater.* **2021**, *33*, No. 2005683.
- (47) Ang, M. C. Y.; Dhar, N.; Khong, D. T.; Lew, T. T. S.; Park, M.; Sarangapani, S.; Cui, J.; Dehadrai, A.; Singh, G. P.; Chan-Park, M. B.; Sarojam, R.; Strano, M. Nanosensor Detection of Synthetic Auxins in Planta Using Corona Phase Molecular Recognition. *ACS Sens.* **2021**, *6*, 3032–3046.
- (48) Boonyaves, K.; Ang, M. C. Y.; Park, M.; Cui, J.; Khong, D. T.; Singh, G. P.; Koman, V. B.; Gong, X.; Porter, T. K.; Choi, S. W.; Chung, K.; Chua, N. H.; Urano, D.; Strano, M. S. Near-Infrared Fluorescent Carbon Nanotube Sensors for the Plant Hormone Family Gibberellins. *Nano Lett.* **2023**, 23, 916–924.

- (49) Iverson, N. M.; Barone, P. W.; Shandell, M.; Trudel, L. J.; Sen, S.; Sen, F.; Ivanov, V.; Atolia, E.; Farias, E.; McNicholas, T. P.; Reuel, N.; Parry, N. M. A.; Wogan, G. N.; Strano, M. S. In Vivo Biosensing via Tissue-Localizable near-Infrared-Fluorescent Single-Walled Carbon Nanotubes. *Nat. Nanotechnol.* **2013**, *8*, 873–880.
- (50) Kruss, S.; Landry, M. P.; Vander Ende, E.; Lima, B. M. A. A.; Reuel, N. F.; Zhang, J.; Nelson, J.; Mu, B.; Hilmer, A.; Strano, M. Neurotransmitter Detection Using Corona Phase Molecular Recognition on Fluorescent Single-Walled Carbon Nanotube Sensors. *J. Am. Chem. Soc.* **2014**, *136*, 713–724.
- (51) Mu, B.; Ahn, J.; McNicholas, T. P.; Strano, M. S. Generating Selective Saccharide Binding Affinity of Phenyl Boronic Acids by Using Single-Walled Carbon Nanotube Corona Phases. *Chem. Eur. J.* **2015**, *21*, 4523–4528.
- (52) Bisker, G.; Bakh, N. A.; Lee, M. A.; Ahn, J.; Park, M.; O'Connell, E. B.; Iverson, N. M.; Strano, M. S. Insulin Detection Using a Corona Phase Molecular Recognition Site on Single-Walled Carbon Nanotubes. *ACS Sens.* **2018**, *3*, 367–377.
- (53) Cho, S.-Y.; Jin, X.; Gong, X.; Yang, S.; Cui, J.; Strano, M. S. Antibody-Free Rapid Detection of SARS-CoV-2 Proteins Using Corona Phase Molecular Recognition to Accelerate Development Time. *Anal. Chem.* **2021**, *93*, 14685–14693.
- (54) Rose-John, S. Interleukin-6 Family Cytokines. *Cold Spring Harbor Perspect. Biol.* **2018**, *10*, No. a028415.
- (55) Tanaka, T.; Narazaki, M.; Kishimoto, T. IL-6 in Inflammation, Immunity, and Disease. *Cold Spring Harbor Perspect. Biol.* **2014**, 6, No. a016295.
- (56) Keystone, E.; Omair, M. A. Interleukin-6 Inhibition. *Rheumatology* **2015**, *1*–2, 485–491.
- (57) Matsuda, T.; Kishimoto, T. Interleukin 6. Encycl. Immunol. 1998, 1458-1461.
- (58) Metcalfe, R. D.; Putoczki, T. L.; Griffin, M. D. W. Structural Understanding of Interleukin 6 Family Cytokine Signaling and Targeted Therapies: Focus on Interleukin 11. Front. Immunol. 2020, 11, 1424.
- (59) Ueki, S.; Le Pham, D.; Gubernatorova, E. O.; Drutskaya, M. S.; Gorshkova, E. A.; Namakanova, O. A.; Zvartsev, R. V.; Hidalgo, J.; Tumanov, A. V.; Nedospasov, S. A. Non-Redundant Functions of IL-6 Produced by Macrophages and Dendritic Cells in Allergic Airway Inflammation. *Front. Immunol.* **2018**, *1*, 2718.
- (60) Legrand-Poels, S.; Schoonbroodt, S.; Piette, J. Regulation of Interleukin-6 Gene Expression by pro-Inflammatory Cytokines in a Colon Cancer Cell Line. *Biochem. J.* **2000**, 349, 765–773.
- (61) Hubackova, S.; Krejcikova, K.; Bartek, J.; Hodny, Z. Interleukin 6 Signaling Regulates Promyelocytic Leukemia Protein Gene Expression in Human Normal and Cancer Cells. *J. Biol. Chem.* **2012**, 287, 26702–26714.
- (62) Scheller, J.; Chalaris, A.; Schmidt-Arras, D.; Rose-John, S. The Pro- and Anti-Inflammatory Properties of the Cytokine Interleukin-6. *Biochim. Biophys. Acta* **2011**, *1813*, 878–888.
- (63) Marques-Deak, A.; Cizza, G.; Eskandari, F.; Torvik, S.; Christie, I. C.; Sternberg, E. M.; Phillips, T. M. Measurement of Cytokines in Sweat Patches and Plasma in Healthy Women: Validation in a Controlled Study. *J. Immunol. Methods* **2006**, *315*, 99–109.
- (64) Arican, O.; Aral, M.; Sasmaz, S.; Ciragil, P. Serum Levels of TNF- $\alpha$ , IFN- $\gamma$ , IL-6, IL-8, IL-12, IL-17, and IL-18 in Patients With Active Psoriasis and Correlation With Disease Severity. *Mediators Inflammation* **2005**, 2005, 273–279.
- (65) Khan, M. A.; Mujahid, M. Recent Advances in Electrochemical and Optical Biosensors Designed for Detection of Interleukin 6. *Sensors* **2020**, *20*, No. 646.
- (66) Said, E. A.; Al-Reesi, I.; Al-Shizawi, N.; Jaju, S.; Al-Balushi, M. S.; Koh, C. Y.; Al-Jabri, A. A.; Jeyaseelan, L. Defining IL-6 Levels in Healthy Individuals: A Meta-Analysis. *J. Med. Virol.* **2021**, *93*, 3915—3924
- (67) Quinn, A. M.; Williams, A. R.; Sivilli, T. I.; Raison, C. L.; Pace, T. W. W. The Plasma Interleukin-6 Response to Acute Psychosocial Stress in Humans Is Detected by a Magnetic Multiplex Assay: Comparison to High-Sensitivity ELISA. *Stress* **2018**, *21*, 376–381.

- (68) Thompson, D. K.; Huffman, K. M.; Kraus, W. E.; Kraus, V. B. Critical Appraisal of Four IL-6 Immunoassays. *PLoS One* **2012**, *7*, No. e30659.
- (69) Adrover-Jaume, C.; Alba-Patiño, A.; Clemente, A.; Santopolo, G.; Vaquer, A.; Russell, S. M.; Barón, E.; González del Campo, M.; Ferrer, J. M.; Berman-Riu, M.; García-Gasalla, M.; Aranda, M.; Borges, M.; de la Rica, R. Paper Biosensors for Detecting Elevated IL-6 Levels in Blood and Respiratory Samples from COVID-19 Patients. Sens. Actuators, B 2021, 330, No. 129333.
- (70) Chen, G.; Wu, D.; Guo, W.; Cao, Y.; Huang, D.; Wang, H.; Wang, T.; Zhang, X.; Chen, H.; Yu, H.; Zhang, X.; Zhang, M.; Wu, S.; Song, J.; Chen, T.; Han, M.; Li, S.; Luo, X.; Zhao, J.; Ning, Q. Clinical and Immunological Features of Severe and Moderate Coronavirus Disease 2019. *J. Clin. Invest.* 2020, 130, 2620–2629.
- (71) Han, H.; Ma, Q.; Li, C.; Liu, R.; Zhao, L.; Wang, W.; Zhang, P.; Liu, X.; Gao, G.; Liu, F.; Jiang, Y.; Cheng, X.; Zhu, C.; Xia, Y. Profiling Serum Cytokines in COVID-19 Patients Reveals IL-6 and IL-10 Are Disease Severity Predictors. *Emerg. Microbes Infect.* **2020**, *9*, 1123–1130.
- (72) Jafrin, S.; Aziz, M. A.; Islam, M. S. Elevated Levels of Pleiotropic Interleukin-6 (IL-6) and Interleukin-10 (IL-10) Are Critically Involved With the Severity and Mortality of COVID-19: An Updated Longitudinal Meta-Analysis and Systematic Review on 147 Studies. *Biomark. Insights* **2022**, *17*, No. 117727192211066.
- (73) Kwon, J. S.; Kim, J. Y.; Kim, M. C.; Park, S. Y.; Kim, B. N.; Bae, S.; Cha, H. H.; Jung, J.; Kim, M. J.; Jin, M. L.; Choi, S. H.; Chung, J. W.; Shin, E. C.; Kim, S. H. Factors of Severity in Patients with COVID-19: Cytokine/Chemokine Concentrations, Viral Load, and Antibody Responses. *Am. J. Trop. Med. Hyg.* **2020**, *103*, 2412–2418.
- (74) Rose-John, S.; Scheller, J.; Schaper, F. "Family Reunion"—A Structured View on the Composition of the Receptor Complexes of Interleukin-6-Type and Interleukin-12-Type Cytokines. *Cytokine Growth Factor Rev.* **2015**, *26*, 471–474.
- (75) Gelinas, A. D.; Davies, D. R.; Edwards, T. E.; Rohloff, J. C.; Carter, J. D.; Zhang, C.; Gupta, S.; Ishikawa, Y.; Hirota, M.; Nakaishi, Y.; Jarvis, T. C.; Janjic, N. Crystal Structure of Interleukin-6 in Complex with a Modified Nucleic Acid Ligand. *J. Biol. Chem.* **2014**, 289, 8720.
- (76) Spangler, J. B.; Moraga, I.; Mendoza, J. L.; Garcia, K. C. Insights into Cytokine-Receptor Interactions from Cytokine Engineering. *Annu. Rev. Immunol.* **2015**, 33, 139–167.
- (77) Liu, Y.; Pollock, K. L.; Cavicchi, K. A. Synthesis of Poly(Trioctylammonium p-Styrenesulfonate) Homopolymers and Block Copolymers by RAFT Polymerization. *Polymer* **2009**, *50*, 6212–6217.
- (78) Dong, J.; Lee, M. A.; Rajan, A. G.; Rahaman, I.; Sun, J. H.; Park, M.; Salem, D. P.; Strano, M. S. A Synthetic Mimic of Phosphodiesterase Type 5 Based on Corona Phase Molecular Recognition of Single-Walled Carbon Nanotubes. *Proc. Natl. Acad. Sci. U.S.A.* 2020, 117, 26616–26625.
- (79) Salem, D. P.; Landry, M. P.; Bisker, G.; Ahn, J.; Kruss, S.; Strano, M. S. Chirality Dependent Corona Phase Molecular Recognition of DNA-Wrapped Carbon Nanotubes. *Carbon* **2016**, 97, 147–153.
- (80) Silmore, K. S.; Gong, X.; Strano, M. S.; Swan, J. W. High-Resolution Nanoparticle Sizing with Maximum a Posteriori Nanoparticle Tracking Analysis. *ACS Nano* **2019**, *13*, 3940–3952.
- (81) Gong, X.; Park, M.; Parviz, D.; Silmore, K. S.; Gordiichuk, P.; Lew, T. T. S.; Strano, M. S. Single-Particle Tracking for Understanding Polydisperse Nanoparticle Dispersions. *Small* **2019**, *15*, No. 1901468.
- (82) Salem, D. P.; Gong, X.; Liu, A. T.; Koman, V. B.; Dong, J.; Strano, M. S. Ionic Strength-Mediated Phase Transitions of Surface-Adsorbed DNA on Single-Walled Carbon Nanotubes. *J. Am. Chem. Soc.* **2017**, *139*, 16791–16802.
- (83) Somers, W.; Stahl, M.; Seehra, J. S. 1.9 Å Crystal Structure of Interleukin 6: Implications for a Novel Mode of Receptor Dimerization and Signaling. *EMBO J.* **1997**, *16*, 989–997.

- (84) Park, M.; Salem, D. P.; Parviz, D.; Gong, X.; Silmore, K. S.; Lew, T. T. S.; Khong, D. T.; Ang, M. C.-Y. Y.; Kwak, S.-Y. Y.; Chan-Park, M. B.; Strano, M. S. Measuring the Accessible Surface Area within the Nanoparticle Corona Using Molecular Probe Adsorption. *Nano Lett.* **2019**, *19*, 7712–7724.
- (85) Gong, X.; Cho, S. Y.; Kuo, S.; Ogunlade, B.; Tso, K.; Salem, D. P.; Strano, M. S. Divalent Metal Cation Optical Sensing Using Single-Walled Carbon Nanotube Corona Phase Molecular Recognition. *Anal. Chem.* **2022**, *94*, 16393–16401.
- (86) Metcalfe, R. D.; Aizel, K.; Zlatic, C. O.; Nguyen, P. M.; Morton, C. J.; Lio, D. S. S.; Cheng, H. C.; Dobson, R. C. J.; Parker, M. W.; Gooley, P. R.; Putoczki, T. L.; Griffin, M. D. W. The Structure of the Extracellular Domains of Human Interleukin  $11\alpha$  Receptor Reveals Mechanisms of Cytokine Engagement. *J. Biol. Chem.* **2020**, 295, 8285–8301.
- (87) Hinds, M. G.; Maurer, T.; Zhang, J. G.; Nicola, N. A.; Norton, R. S. Solution Structure of Leukemia Inhibitory Factor. *J. Biol. Chem.* 1998, 273, 13738–13745.
- (88) Di Marco, A.; Gloaguen, I.; Graziani, R.; Paonessa, G.; Saggio, I.; Hudson, K. R.; Laufer, R. Identification of Ciliary Neurotrophic Factor (CNTF) Residues Essential for Leukemia Inhibitory Factor Receptor Binding and Generation of CNTF Receptor Antagonists. *Proc. Natl. Acad. Sci. U.S.A.* 1996, 93, 9247–9252.
- (89) Yohannes, G.; Wiedmer, S. K.; Elomaa, M.; Jussila, M.; Aseyev, V.; Riekkola, M. L. Thermal Aggregation of Bovine Serum Albumin Studied by Asymmetrical Flow Field-Flow Fractionation. *Anal. Chim. Acta* **2010**, *675*, 191–198.
- (90) Lundberg, D. J.; Strano, M. S. Approximate Corona Phase Hamiltonian for Individual Cylindrical Nanoparticle—Polymer Interactions. *J. Phys. Chem. B* **2022**, *126*, 347–354.
- (91) Bisker, G.; Ahn, J.; Kruss, S.; Ulissi, Z. W.; Salem, D. P.; Strano, M. S. A Mathematical Formulation and Solution of the CoPhMoRe Inverse Problem for Helically Wrapping Polymer Corona Phases on Cylindrical Substrates. *J. Phys. Chem. C* **2015**, *119*, 13876–13886.
- (92) Hirose, E.; Iwamoto, Y.; Norisuye, T. Chain Stiffness and Excluded-Volume Effects in Sodium Poly(Styrenesulfonate) Solutions at High Ionic Strength. *Macromolecules* 1999, 32, 8629–8634.
- (93) Durchschlag, H.; Puchwein, G.; Kratky, O.; Breitenbach, J. W.; Olaj, O. F. Small-Angle and Wide-Angle X-Ray Investigations on Poly-m-Bromostyrene and Poly-o-Bromostyrene in Benzene Solution. *J. Polym. Sci., Part C: Polym. Symp.* **2007**, *31*, 311–343.
- (94) Jarosch, R. The Alpha-Helix, an Overlooked Molecular Motor. *Protoplasma* **2005**, 227, 37–46.
- (95) Andrews, D. W.; Ottensmeyer, F. P. Electron Microscopy of the Poly-L-Lysine Alpha-Helix. *Ultramicroscopy* **1982**, *9*, 337–348.
- (96) Gugoasa, L. A.; Stefan-Van Staden, R. I.; Dima, A.; Visan, C. A.; Streinu-Cercel, A.; Biris, A.; Calenic, B. Fast Screening of Biological Fluids for Cytokines and Adipokines Using Stochastic Sensing. *Microelectron. Eng.* **2015**, *148*, 64–69.
- (97) Pirsean, C.; Neguirt, C.; Stefan-van Staden, R. I.; Dinu-Pirvu, C. E.; Armean, P.; Udeanu, D. I. The Salivary Levels of Leptin and Interleukin-6 as Potential Inflammatory Markers in Children Obesity. *PLoS One* **2019**, *14*, No. e0210288.
- (98) Negut, C. C.; van Staden, R. I. S.; Ungureanu, E. M.; Udeanu, D. I. Stochastic Sensors Designed for Assessment of Biomarkers Specific to Obesity. *J. Pharm. Biomed. Anal.* **2016**, *128*, 280–285.
- (99) Jin, H.; Heller, D. A.; Kim, J.-H.; Strano, M. S. Stochastic Analysis of Stepwise Fluorescence Quenching Reactions on Single-Walled Carbon Nanotubes: Single Molecule Sensors. *Nano Lett.* **2008**, *8*, 4299–4304.
- (100) Bakh, N. A.; Gong, X.; Lee, M. A.; Jin, X.; Koman, V. B.; Park, M.; Nguyen, F. T.; Strano, M. S. Transcutaneous Measurement of Essential Vitamins Using Near-Infrared Fluorescent Single-Walled Carbon Nanotube Sensors. *Small* **2021**, *17*, No. 2100540.